Numerical Investigations of Fractional Complex Coupled Maccari and Cahn-Hilliard Equations Using Controlled Picard Iteration with ρ-Laplace Transform

Nauman Raza[1,2,*], Zuha Khalid[1], Younes Chahlaoui[3], Muhammad Farman[2,4] and Evren Hincal[2,4]

[1] Institute of Mathematics, University of the Punjab, Quaid-e-Azam Campus, Lahore, 54590, Pakistan

[2] Mathematics Research Center, Near East University, Near East Boulevard, Nicosia, Mersin 10, 99138, Turkey

[3] Department of Mathematics, College of Science, King Khalid University, Abha, 61413, Saudi Arabia

[4] Research Center of Applied Mathematics, Khazar University, Baku, 1009, Azerbaijan

INFORMATION

Keywords:
Generalized caputo fractional derivative
fractional complex coupled maccari system
cahn-hilliard equation
controlled picard technique
laplace transform method

DOI: 10.23967/j.rimni.2025.10.65937

SCIPEDIA Revista Internacional de Métodos Numéricos para Cálculo y Diseño en Ingeniería

RIMNI Revista Internacional Métodos numéricos para cálculo y diseño en ingeniería

Numerical Investigations of Fractional Complex Coupled Maccari and Cahn-Hilliard Equations Using Controlled Picard Iteration with ρ-Laplace Transform

Nauman Raza[1,2,*], **Zuha Khalid**[1], **Younes Chahlaoui**[3], **Muhammad Farman**[2,4] **and Evren Hincal**[2,4]

[1]Institute of Mathematics, University of the Punjab, Quaid-e-Azam Campus, Lahore, 54590, Pakistan

[2]Mathematics Research Center, Near East University, Near East Boulevard, Nicosia, Mersin 10, 99138, Turkey

[3]Department of Mathematics, College of Science, King Khalid University, Abha, 61413, Saudi Arabia

[4]Research Center of Applied Mathematics, Khazar University, Baku, 1009, Azerbaijan

ABSTRACT

This article presents a semi-analytical approach to address two nonlinear evolution equations: the fractional complex coupled Maccari system and the fractional Cahn-Hilliard equation. These mathematical models encapsulate essential concepts such as non-locality and memory, making them applicable in signal and image processing. The proposed method utilizes the controlled Picard framework combined with the ρ-Laplace transform. The recommended approach eliminates the necessity for traditional techniques, such as Lagrange multipliers and Adomian expansions, by integrating the controlled Picard method with the ρ-Laplace transformation. Additionally, a minimal parameter, ħ, has been introduced to improve the convergence of the system under investigation. The results have been validated against exact solutions, and absolute error analyses support the accuracy of the proposed approach. The article includes 2D and 3D plots to illustrate how results vary with different parameters. In conclusion, this paper demonstrates that our method is explicit and efficiently executable.

OPEN ACCESS

Received: 25/03/2025

Accepted: 07/05/2025

Published: 30/05/2025

DOI
10.23967/j.rimni.2025.10.65937

Keywords:
Generalized caputo fractional derivative
fractional complex coupled maccari system
cahn-hilliard equation
controlled picard technique
laplace transform method

1 Introduction

The proposition of fractional calculus (FC) is to take ordinary differential equations and modify them by the introduction of non-integer order derivatives; thus making itself a major pillar for more complex mathematical representations [1]. For this reason, FC has gained popularity among image processing experts because it is capable of enhancing high-frequency transmission signals while at the same time amplifying signals in the middle range and retaining low voltages through non-linear

*Correspondence: Nauman Raza (nauman.math@pu.edu.pk).

transformations [2,3]. In engineering circles, FC has been used to optimize electromagnetic systems, derive control theory frameworks, and ignite signal processing development, thus leading to efficient antennas and filters [4]. Biomedicine applies FC in simulating biological systems functioning like nerve conduction mechanisms, including drug release kinetics and bioelectrical impedance analysis [5]. On economic fronts, even though gross domestic product models have been improved on by FC, it has also contributed towards enhancing memory processes for asset prices as well as good risk management techniques; hence, this could be seen as a leap forward [6,7]. All areas of research benefiting from this are testimony to how much FC can influence methodological innovations across diverse fields or domains.

Nonlinear evolution equations (NLEEs) preside over the time dependent behavior of a function $u(\theta, \mathrm{t})$, generally associating the latter with its spatial derivatives. Given that $u(\theta, 0)$ is rapidly decaying at infinity, one turns to determine the evolution of the same function over time [8,9]. Many intricate phenomena are explained by NLEEs, which hold significant relevance in various areas of science and engineering. For instance, the Korteweg-de Vries (KdV) equation embodies shallow water waves and plasma waves, while the Navier-Stokes equations offer models for turbulence, ocean currents, and air flows. Wave evolution in optical fibers and Bose-Einstein condensates is governed by the nonlinear Schrödinger equation, which encapsulates essential nonlinear effects. Moreover, waves generated by shocks due to traffic movement or turbulence are modeled using Burgers' equation [10].

Our study investigates two NLEEs: the fractional complex coupled Maccari system (FCCMS) and the fractional Cahn-Hilliard equation (FCHE). Maccari first introduced the Maccari system in 1996, deriving it from the Kadomtsev-Petviashvili problem using Fourier expansion and adjustments in the spatiotemporal scale [11]. To analyze the impact of fractional dynamics, we reformulated the complex coupled Maccari system into its fractional counterpart, the FCCMS, which is represented as [12]:

$$\begin{cases} \iota D_{\mathrm{t}}^{\alpha,\rho} f + f_{\theta\theta} + fg = 0, \\ D_{\mathrm{t}}^{\alpha,\rho} g + g_{y} + (|f|^2)_{\theta} = 0, \quad \rho > 0, \quad 0 < \alpha \leq 1, \quad \iota = \sqrt{-1}, \end{cases} \tag{1}$$

here, $f = f(\theta, y, t)$ denotes the complex scalar field, and $g = g(\theta, y, t)$ describes the real scalar field. The imaginary unit is given as $\iota = \sqrt{-1}$. Moreover, $D_{\mathrm{t}}^{\alpha,\rho}$ indicates the generalized Caputo fractional derivative (GCFD) having α as the order, in relation to time and parameter ρ, which is a positive real. The Maccari system is a basic model in nonlinear wave physics, being integrable and having soliton solutions. An integrable system admits exact analytical solutions; therefore, it is a key system for studying nonlinear wave dynamics. The Maccari system's soliton solutions are crucial for understanding stable wave propagation and interactions that are significant in various physical applications. In addition, the Maccari system acts as a unifying connection between different classes of NLEEs to explain the underlying mathematical structures behind complex wave events. The FCCMS provides a theoretical framework for studying nonlinear wave interactions, solitons, and instability phenomena in optical fibers. Its applications span telecommunications, laser technology, signal processing, and nonlinear optics, making it a valuable tool for advancing fiber-optic technologies. In plasma physics, the FCCMS effectively models nonlinear waves (e.g., solitons, shocks, rogue waves), multi-species plasma behavior (including dusty and quantum plasmas), and processes like turbulence, energy transport, and electromagnetic wave-plasma interactions. It is relevant in a wide range of subjects such as fluid dynamics, optical wave propagation, quantum systems, biology, astrophysics, and fields where non-linear features dominate [13].

The Cahn-Hilliard equation, a fourth-order partial differential equation, follows a parabolic structure, was put forward in 1958 based on ideas of Cahn and Hilliard [14] to depict phase separation in binary alloys at their critical temperature. It has been widely analyzed both mathematically and computationally [15]. Here we will be extending our examination towards FCHE based on fractional dynamics given by:

$$D_{\mathrm{t}}^{\alpha,\rho} f + f_{\theta\theta\theta\theta} - (f^3 - f)_{\theta\theta} - \beta f_{\theta} = 0, \quad \rho > 0, \quad 0 < \alpha \leq 1. \tag{2}$$

β is the key parameter indicating the strength of advection, which assesses how strongly the system is influenced by a direction, either suppressing or enhancing the typical diffusive behavior. The FCHE models phase separation and pattern formation in diverse systems. It explains spinodal decomposition in alloys/polymers, grain growth in metals, and thin film dynamics in materials science; block copolymer self-assembly in soft matter; binary fluid mixing in fluid dynamics; tumor growth and cell sorting in biology; and image denoising. Emerging uses include 3D printing, battery materials, and neuroscience. This mass-conserving equation uniquely describes microstructure evolution through nonlinear diffusion, bridging physics, engineering, and biology [16,17].

Models of this kind are very important in understanding materials with intricate interaction, nanomaterials, and systems that are influenced by temperature fluctuations or noise. Fractional derivatives allow for a better portrayal of realistic dynamics than standard models do. A great deal of research has gone into the FCCMS and FCHE, with researchers using a myriad of methods to study their solutions. It involves the Bernoulli sub-ODE (BS-ODE) approach, the generalized Kudryashov (GK) method [18], exp $(-\phi(\xi))$-expansion method, the sine-cosine method [19], and q-homotopy analysis method [20]. This investigation focuses on introducing a novel semi-analytical framework to obtain time-dependent solutions for the FCCMS and FCHE. To address their complexity, the approach combines the Controlled Picard (CP) method with the ρ-Laplace transform (LT) method using GCFD. This iterative methodology effectively refines an initial approximation, facilitating convergence toward the precise solution. By employing LT, the equations are reformulated into a set of algebraic expressions, streamlining the computational process and enhancing efficiency. Significantly, this work represents the first use of the GCFD with the parameter ρ to solve the proposed model. This method greatly enhances the ability to explore the system's underlying behavior. By utilizing this innovative semi-analytical approach, researchers can obtain a deeper understanding of the models' dynamics, structure, and predictive characteristics. The results of this research may significantly contribute to the development of theoretical frameworks in physics and applied mathematical modeling, which have implications across numerous scientific fields.

The paper is organized into well-defined sections to ensure a clear presentation of our study. Section 2 introduces the fundamental concepts and terminology of FC. Section 3 elaborates on the outlined methodology, which integrates the ρ-LT with the CP method. In Section 4, we exhibit the practical implication of the methodology to the introduced models, emphasizing its effectiveness. Section 5 provides a graphical visualization of the results to support the findings. Lastly, the paper concludes by highlighting the core insights and contributions, underscoring the importance of this research.

2 Preliminaries

This segment presents a concise and precise overview of the fundamental definitions pertinent to FC, laying the groundwork for the subsequent analysis.

Definition 1. The work presented in [21] introduces an innovative fractional integral operator of order α designed for application to the function $f : [0, +\infty) \to \mathbb{R}$, defined as follows:

$$(\Im^{\alpha,\rho} f)(\mathrm{t}) = \frac{\rho^{1-\alpha}}{\Gamma(\alpha)} \int_0^{\mathrm{t}} \frac{\xi^{\rho-1} f(\xi)}{(\mathrm{t}^{\rho} - \xi^{\rho})^{1-\alpha}} d\xi. \tag{3}$$

In this context, the gamma function, denoted by $\Gamma(.)$, is defined under the conditions $\rho > 0$, $\mathrm{t} > 0$, and $0 < \alpha \leq 1$, ensuring that the established requirements are satisfied.

Definition 2. For a function $f : [0, +\infty) \to \mathbb{R}$, GCFD of order α is formally defined as [21,22]:

$$({}^{C}D^{\alpha,\rho} f)(\mathrm{t}) = \frac{1}{\Gamma(n-\alpha)} \int_0^{\mathrm{t}} (\mathrm{t} - \xi)^{n-\alpha-1} f^{(n)}(\xi) d\xi, \tag{4}$$

where $\rho > 0$ and $0 < \alpha \leq 1$.

Definition 3. The ρ-LT, applicable to a function f continuous on the interval $[0, +\infty)$, is rigorously defined as [23]:

$$\mathcal{L}_{\rho} f(t)(s) = \int_0^{\infty} e^{-s\frac{\mathrm{t}^{\rho}}{\rho}} f(\mathrm{t}) \frac{d\mathrm{t}}{\mathrm{t}^{1-\rho}}. \tag{5}$$

The ρ-LT of a function f associated with the GCFD is succinctly presented in [23]:

$$\mathcal{L}_{\rho}\{({}^{C}D^{\alpha,\rho} f)(\mathrm{t})\} = s^{\alpha}\mathcal{L}_{\rho}\{f(\mathrm{t})\} - \sum_{\ell=0}^{n-1} s^{\alpha-\ell-1} f^{\ell}(0). \tag{6}$$

Lemma 1: The essential properties of the ρ-LT are presented below [24]:

1. $\mathcal{L}_{\rho}\{1\}(s) = \dfrac{1}{s}, s > 0.$
2. $\mathcal{L}_{\rho}\{\mathrm{t}^{\eta}\}(s) = \rho^{\frac{\eta}{\rho}} \dfrac{\Gamma\left(1 + \frac{\eta}{\rho}\right)}{s^{1+\frac{\eta}{\rho}}}, \quad \eta \in \mathbb{R}, \quad s > 0.$
3. $\mathcal{L}_{\rho}\{e^{\lambda \frac{\mathrm{t}^{\rho}}{\rho}}\}(s) = \dfrac{1}{s - \lambda}, s > 0.$

3 Fundamental Concept of Controlled Picard's Technique Using ρ-Laplace Transform

The formulated methodology integrates the CP method with the ρ-LT approach. Emile Picard was the first person to give the idea of the Picard scheme back in 1890; it is a versatile tool for solving initial value problems. To address challenges with convergence and the rate of approximation in Picard's method, Semary et al. [25] introduced an enhancement that incorporates a complementary parameter, resulting in the CP method. This approach demonstrates a substantial reduction in computational workload compared to conventional methods. While implementing the CP method may present challenges due to the parameter $\hbar$, it consistently delivers precise numerical results. The reduction in computational work significantly enhances the efficiency of the approach. We will now rigorously analyze the general form that follows:

$$D_{\mathrm{t}}^{\alpha,\rho} f(\theta, \mathrm{t}) + \aleph[f(\theta, \mathrm{t})] + \mathrm{L}[f(\theta, \mathrm{t})] = \nu(\theta, \mathrm{t}), \quad \rho > 0,\ 0 < \alpha \leq 1, \tag{7}$$

under the given initial conditions:

$$f(\theta,0)=\phi_0(\theta). \tag{8}$$

In this formulation, ν denotes a non-homogeneous source term, while the differential operators L and $\aleph$ correspond to linear and nonlinear components, respectively, involving partial derivatives concerning the spatial variable θ, thereby reflecting the α order GCFD. Additionally, there exists a complex-valued function $f(\theta,\mathrm{t})$ that requires determination.

To optimize the application of the CP technique in conjunction with the ρ-LT, Eq. (7) is restructured as follows:

$$D_{\mathrm{t}}^{\alpha,\rho}f(\theta,\mathrm{t})+\aleph[f(\theta,\mathrm{t})]+\mathrm{L}[f(\theta,\mathrm{t})]-\nu(\theta,\mathrm{t})=0. \tag{9}$$

To analyze Eq. (9), we first employ the ρ-LT, leveraging its linearity and the known fractional derivative properties. This transformation converts the equation into an algebraic form:

$$\mathcal{L}_\rho\{D_{\mathrm{t}}^{\alpha,\rho}f(\theta,\mathrm{t})\}+\mathcal{L}_\rho\{\aleph[f(\theta,\mathrm{t})]+\mathrm{L}[f(\theta,\mathrm{t})]-\nu(\theta,\mathrm{t})\}=0. \tag{10}$$

In accordance with the stated Definition 3, Eq. (10) may be restated as follows:

$$s^\alpha\mathcal{L}_\rho\{f(\theta,\mathrm{t})\}-\sum_{\ell=0}^{n-1}s^{\alpha-\ell-1}f^{(\ell)}(\theta,0)+\mathcal{L}_\rho\{\aleph[f(\theta,\mathrm{t})]+\mathrm{L}[f(\theta,\mathrm{t})]-\nu(\theta,\mathrm{t})\}=0. \tag{11}$$

We will now implement Picard's method,

$$s^\alpha\mathcal{L}_\rho\{f_{m+1}(\theta,\mathrm{t})\}=\sum_{\ell=0}^{n-1}s^{\alpha-\ell-1}f^{(\ell)}(\theta,0)-\mathcal{L}_\rho\{\aleph[f_m(\theta,\mathrm{t})]+\mathrm{L}[f_m(\theta,\mathrm{t})]-\nu(\theta,\mathrm{t})\}. \tag{12}$$

The results have been thoughtfully derived by strategically adding and subtracting the terms $\mathcal{L}_\rho D_{\mathrm{t}}^{\alpha,\rho}f_m(\theta,\mathrm{t})$ to the right side of Eq. (12):

$$\begin{aligned}s^\alpha\mathcal{L}_\rho\{f_{m+1}(\theta,\mathrm{t})\}&=\mathcal{L}_\rho D_{\mathrm{t}}^{\alpha,\rho}f_m(\theta,\mathrm{t})+\sum_{\ell=0}^{n-1}s^{\alpha-\ell-1}f^{(\ell)}(\theta,0)\\&\quad-\mathcal{L}_\rho D_{\mathrm{t}}^{\alpha,\rho}f_m(\theta,\mathrm{t})-\mathcal{L}_\rho\{\aleph[f_m(\theta,\mathrm{t})]+\mathrm{L}[f_m(\theta,\mathrm{t})]-\nu(\theta,\mathrm{t})\}.\end{aligned} \tag{13}$$

After employing the inverse ρ-LT, we obtain the following results as:

$$f_{m+1}(\theta,\mathrm{t})=f_m(\theta,\mathrm{t})-\mathcal{L}_\rho^{-1}\left[\frac{1}{s^\alpha}\mathcal{L}_\rho\left\{D_{\mathrm{t}}^{\alpha,\rho}f_m(\theta,\mathrm{t})+\aleph[f_m(\theta,\mathrm{t})]+\mathrm{L}[f_m(\theta,\mathrm{t})]-\nu(\theta,\mathrm{t})\right\}\right]. \tag{14}$$

$$\Psi\left(\theta,\mathrm{t},f(\theta,\mathrm{t}),\alpha\right)=D_{\mathrm{t}}^{\alpha,\rho}f(\theta,\mathrm{t})+\aleph[f(\theta,\mathrm{t})]+\mathrm{L}[f(\theta,\mathrm{t})]-\nu(\theta,\mathrm{t})=0. \tag{15}$$

Using Eq. (15) and multiplying $\hbar$ on both sides:

$$\hbar\Psi\left(\theta,\mathrm{t},f(\theta,\mathrm{t}),\alpha\right)=0. \tag{16}$$

The term $D_{\mathrm{t}}^{\alpha,\rho}f(\theta,\mathrm{t})$ is added and subtracted to the right of the Eq. (16) to obtain:

$$D_{\mathrm{t}}^{\alpha,\rho}f(\theta,\mathrm{t})+\hbar\Psi\left(\theta,\mathrm{t},f(\theta,\mathrm{t}),\alpha\right)-D_{\mathrm{t}}^{\alpha,\rho}f(\theta,\mathrm{t})=0. \tag{17}$$

Eq. (14) is subjected to Picard's transform iterative formula, which yields:

$$f_{m+1}(\theta,\mathrm{t}) = f_m(\theta,\mathrm{t}) - \mathcal{L}_\rho^{-1}\left[\frac{\hbar}{s^\alpha}\mathcal{L}_\rho\left\{D_\mathrm{t}^{\alpha,\rho} f_m(\theta,\mathrm{t}) + \aleph[f_m(\theta,\mathrm{t})] + \mathrm{L}[f_m(\theta,\mathrm{t})] - \nu(\theta,\mathrm{t})\right\}\right], \tag{18}$$

and the initial conditions are given by:

$$\phi_0(\theta) = \mathcal{L}_\rho^{-1}\left[\frac{1}{s^\alpha}\left[\sum_{\ell=0}^{n-1} s^{\alpha-\ell-1} f^{(\ell)}(\theta,0)\right]\right]. \tag{19}$$

Eq. (14) establishes an iterative framework for approximating solutions to Eq. (9) across both fractional and integer orders. At this stage, an auxiliary parameter, denoted as $\hbar$, is introduced into the Picard iterative transformation to improve the control over the convergence domain of the predicted solutions for Eq. (9). Consequently, we now investigate Eq. (9) as shown below:

$$f_{m+1}(\theta,\mathrm{t}) = (1-\mathrm{h})f_m(\theta,\mathrm{t}) + \mathrm{h}f_m(\theta,0) - \mathrm{h}\mathcal{L}_\rho^{-1}\left[\frac{1}{s^\alpha}\mathcal{L}_\rho\left\{\aleph[f_m(\theta,\mathrm{t})] + \mathrm{L}[f_m(\theta,\mathrm{t})] - \nu(\theta,\mathrm{t})\right\}\right]. \tag{20}$$

Using Mathematica 13.2, we begin with initial approximations ϕ_0 that fulfill the initial conditions and compute $f_{m+1}(\theta,\mathrm{t})$. The unknown value of $\hbar$ is determined through the $\hbar$-curve technique, as outlined in [25]. This method identifies the horizontal region corresponding to the acceptable range of $\hbar$, ensuring the convergence of the solution.

4 Applications

This section will demonstrate the effectiveness and broad applicability of our approach through its application to FCCMS and FCHE.

4.1 Numerical Solution of Time-FCCMS

Recalling Eq. (1), it can be simplified as:

$$\begin{cases} D_\mathrm{t}^{\alpha,\rho} f - \iota f_{\theta\theta} - \iota f g & = 0, \\ D_\mathrm{t}^{\alpha,\rho} g + g_y + (f\bar{f})_\theta & = 0, \end{cases} \tag{21}$$

where $0 < \alpha \leq 1$ and $|f|^2 = f\bar{f}$, while $\bar{f}$ is the conjugate of the function f.

Subject to initial conditions:

$$\begin{aligned} f(\theta,y,0) &= \sqrt{\frac{a+1}{2}}\alpha \tanh\left[\frac{1}{2}\alpha(\theta+y)\right] e^{i(\xi\theta+\eta y)}, \\ g(\theta,y,0) &= -\frac{1}{2}\alpha^2 \tanh^2\left[\frac{1}{2}\alpha(\theta+y)\right]. \end{aligned} \tag{22}$$

Using the CP method and the ρ-LT scheme, we obtain the recurrence relations outlined below:

$$\begin{aligned} f_{m+1}(\theta,\mathrm{t},\hbar) &= (1-\hbar)f_m(\theta,\mathrm{t}) + \hbar f_m(\theta,0) + \hbar\mathcal{L}^{-1}\left\{\frac{1}{s^\alpha}\mathcal{L}\{\iota(f_m)_{\theta\theta} + \iota f_m g_m\}\right\}, \\ g_{m+1}(\theta,\mathrm{t},\hbar) &= (1-\hbar)g_m(\theta,\mathrm{t}) + \hbar g_m(\theta,0) - \hbar\mathcal{L}^{-1}\left\{\frac{1}{s^\alpha}\mathcal{L}\{(g_m)_y + (f_m\bar{f}_m)_\theta\}\right\}. \end{aligned} \tag{23}$$

By substituting $m = 0$ into Eq. (23), we derive the following expressions:

$$f_1(\theta,\mathrm{t},\hbar) = (1-\hbar)f_0(\theta,\mathrm{t}) + \hbar f_0(\theta,0) + \hbar\mathcal{L}^{-1}\left\{\frac{1}{s^\alpha}\mathcal{L}\{\iota(f_0)_{\theta\theta} + \iota f_0 g_0\}\right\}, \tag{24}$$

$$g_1(\theta,\mathrm{t},\hbar) = (1-\hbar)g_0(\theta,\mathrm{t}) + \hbar g_0(\theta,0) - \hbar\mathcal{L}^{-1}\left\{\frac{1}{s^\alpha}\mathcal{L}\{(g_0)_y + (f_0\bar{f}_0)_\theta\}\right\}.$$

Using Mathematica 13.2, we can evaluate $f_1(\theta,\mathrm{t},\hbar)$ and $g_1(\theta,\mathrm{t},\hbar)$ which are presented below:

$$f_1(\theta,\mathrm{t},\hbar) = \frac{\sqrt{a+1}\alpha sech^2\left(\frac{1}{2}\alpha(\theta+y)\right)e^{i(\xi\theta+\eta y)}}{4\sqrt{2}\Gamma(\alpha+1)} \tag{25}$$
$$\left[-4\alpha\hbar\xi\left(\frac{t^\rho}{\rho}\right)^\alpha + \sinh(\alpha(\theta+y))\left(2\Gamma(\alpha+1) - i\hbar\left(\alpha^2+2\xi^2\right)\left(\frac{\mathrm{t}^\rho}{\rho}\right)^\alpha\right)\right],$$

$$g_1(\theta,\mathrm{t},\hbar) = -\frac{2\alpha^2\sinh^4\left(\frac{1}{2}\alpha(\theta+y)\right)\mathrm{csch}^2(\alpha(\theta+y))\left(2a\hbar\left(\frac{\mathrm{t}^\rho}{\rho}\right)^\alpha\mathrm{csch}(\alpha(\theta+y)) + \Gamma(\alpha)\right)}{\Gamma(\alpha)}.$$

Similarly, by setting $m = 0$ in Eq. (23), we obtain:

$$f_2(\theta,\mathrm{t},\hbar) = (1-\hbar)f_1(\theta,\mathrm{t}) + \hbar f_0(\theta,0) + \hbar\mathcal{L}^{-1}\left\{\frac{1}{s^\alpha}\mathcal{L}\{\iota(f_1)_{\theta\theta} + \iota f_1 g_1\}\right\}, \tag{26}$$

$$g_2(\theta,\mathrm{t},\hbar) = (1-\hbar)g_1(\theta,\mathrm{t}) + \hbar g_0(\theta,0) - \hbar\mathcal{L}^{-1}\left\{\frac{1}{s^\alpha}\mathcal{L}\{(g_1)_y + (f_1\bar{f}_1)_\theta\}\right\}.$$

Through Mathematica 13.2, we assess $f_2(\theta,\mathrm{t},\hbar)$ and $g_2(\theta,\mathrm{t},\hbar)$ as shown below:

$$\begin{aligned}
f_2(\theta,\mathrm{t},\hbar) = {} & \frac{\sqrt{a+1}\alpha e^{i(\xi\theta+\eta y)}}{16\sqrt{2}\Gamma(\alpha)\Gamma(\alpha+1)\Gamma(3\alpha+1)}\left(4(\hbar-1)\mathrm{sech}^2\left[\frac{1}{2}\alpha(\theta+y)\right]\right.\\
& \left(-2\sinh[\alpha(\theta+y)]\frac{\hbar\left(\frac{\mathrm{t}^\rho}{\rho}\right)^\alpha\left(4\alpha\xi + i\left(\alpha^2+2\xi^2\right)\sinh[\alpha(\theta+y)]\right)}{\Gamma(\alpha+1)}\right)\\
& + 16\hbar\tanh\left[\frac{1}{2}\alpha(\theta+y)\right] + \hbar\left(\frac{t^\rho}{\rho}\right)^\alpha\mathrm{sech}^3\left[\frac{1}{2}\alpha(\theta+y)\right]\\
& + \left(2\left(\hbar\left(\frac{\mathrm{t}^\rho}{\rho}\right)^{2\alpha}\left(2i\Gamma(\alpha+1)^2\left(a\alpha + 2\alpha\xi + 2i\xi^2\sinh[\alpha(\theta+y)]\right)\right.\right.\right.\\
& \left.\left.\left. - a\alpha^2\hbar\Gamma(2\alpha+1)\mathrm{sech}^4\left[\frac{1}{2}\alpha(\theta+y)\right]\left(\left(\alpha^2+2\xi^2\right)\sinh[\alpha(\theta+y)] - 4i\alpha\xi\right)\right)\tanh\left[\frac{1}{2}\alpha(\theta+y)\right]\right.\right.\\
& \left.\left. - i\Gamma(\alpha)\left(\hbar\Gamma(\alpha+1)\left(a\alpha^2 - 4\xi^3\right)\left(\frac{\mathrm{t}^\rho}{\rho}\right)^{2\alpha}\sinh[\alpha(\theta+y)]\right.\right.\right.\\
& \left.\left.\left. + 4\left(\alpha^2+2\xi^2\right)\Gamma(3\alpha+1)\tanh\left[\frac{1}{2}\alpha(\theta+y)\right]\right)\right)\right),
\end{aligned} \tag{27}$$

$$g_2(\theta,\mathrm{t},\hbar)=\frac{\alpha^2}{16}\left(\frac{32(\hbar-1)\sinh^4\left[\frac{1}{2}\alpha(\theta+y)\right]\operatorname{csch}^2[\alpha(\theta+y)]\left(2a\hbar\left(\frac{\mathrm{t}^\rho}{\rho}\right)^\alpha\operatorname{csch}[\alpha(\theta+y)]+\Gamma(\alpha)\right)}{\Gamma(\alpha)}\right.$$
$$-8\hbar\tanh^2\left[\frac{1}{2}\alpha(\theta+y)\right]+\hbar\left(\frac{\mathrm{t}^\rho}{\rho}\right)^\alpha\operatorname{sech}^4\left[\frac{1}{2}\alpha(\theta+y)\right]$$
$$\left(\frac{4\alpha^2\hbar(2(a+1)\xi+a)\left(\frac{\mathrm{t}^\rho}{\rho}\right)^\alpha(\cosh[\alpha(\theta+y)]-2)}{\Gamma(2\alpha+1)}+\frac{4a\sinh[\alpha(\theta+y)]}{\Gamma(\alpha)}\right.$$
$$\left.\left.+\frac{(a+1)\alpha\hbar^2\Gamma(2\alpha+1)\left(\frac{t^\rho}{\rho}\right)^{2\alpha+1}\left(\left(\alpha^2+2\xi^2\right)^2\sinh[\alpha(\theta+y)]-16\alpha^2\xi^2\tanh\left[\frac{1}{2}\alpha(\theta+y)\right]\right)}{\Gamma(\alpha+1)^2\Gamma(3\alpha+2)}\right)\right).$$

Using a similar approach, we estimate solutions by varying m specifically $m=2,3,\ldots$, but we will restrict our attention on evaluating $f_2(\theta,\mathrm{t},\hbar)$ and $g_2(\theta,\mathrm{t},\hbar)$. To determine the region of convergence, $\hbar$ curves are plotted at $\mathrm{t}=0.1$ for various α values. A detailed comparison of our approximations and absolute errors for different x values and time steps, alongside the analytical results from [18], is shown in Tables 1 and 2, confirming the CP's efficacy in solving NLEEs.

Table 1: The exact solution in [18] and the numerical approximations of $f(\theta,y,\mathrm{t})$ presented in Eq. (21) and the error magnitude at $a=0.05$, $y=10$, $\rho=1$, $\xi=2.5$, $\eta=1.5$, $\gamma=2$ for $\alpha=1$ at $\hbar=0.3$

t	x	Exact	Numerical	$\lvert Error\rvert$
0.1	–10	–0.00169	0.03169	3.33756×10^{-2}
	–6	0.68471	0.69518	1.04771×10^{-2}
	–1	0.71793	0.71594	1.99821×10^{-3}
	0.2	–0.72449	–0.68768	3.68145×10^{-2}
0.01	–10	–0.00015	0.00319	3.34347×10^{-3}
	–6	0.69837	0.69823	1.48038×10^{-4}
	–1	0.72361	0.72211	1.49953×10^{-3}
	0.2	–0.71175	–0.70678	4.97097×10^{-3}
0.05	–10	–0.00081	0.01590	1.67074×10^{-2}
	–6	0.69508	0.69700	1.92589×10^{-3}
	–1	0.72398	0.71937	4.60796×10^{-3}
	0.2	–0.72030	–0.69830	2.20015×10^{-2}

Table 2: The exact solution in [18] and the numerical approximations of $g(\theta, y, t)$ presented in Eq. (21) and the error magnitude at $a = 0.05$, $y = 10$, $\rho = 1$, $\xi = 2.5$, $\eta = 1.5$, $\gamma = 2$ for $\alpha = 1$ at $\hbar = 0.3$

t	x	Exact	Numerical	$\lvert Error \rvert$
0.1	–10	–0.49990	–0.49991	4.9027×10^{-7}
	–6	–0.49479	–0.49482	2.65134×10^{-5}
	–1	–0.09690	–0.09790	1.00224×10^{-3}
	0.2	–0.00804	–0.00779	2.55618×10^{-4}
0.01	–10	–0.49991	–0.49991	6.12682×10^{-8}
	–6	–0.49481	–0.49482	3.31403×10^{-6}
	–1	–0.09770	–0.09782	1.28701×10^{-4}
	0.2	–0.00776	–0.00773	2.965×10^{-5}
0.05	–10	–0.49990	–0.49991	2.54936×10^{-7}
	–6	–0.49480	–0.49482	1.37879×10^{-5}
	–1	–0.09734	–0.09787	5.2703×10^{-4}
	0.2	–0.00789	–0.00776	1.29019×10^{-4}

4.2 Numerical Solution of Time-FCHE

Recalling Eq. (2) having the initial conditions:

$$f(\theta, 0) = \tanh\left(\frac{\theta}{\sqrt{2}}\right). \tag{28}$$

Applying the CP method and the ρ-LT strategies obtained from Eq. (20) to the Eq. (2) allows us to establish the following recurrence relations:

$$f_{m+1}(\theta, t, \hbar) = (1-\hbar) f_m(\theta, t) + \hbar f_m(\theta, 0) - \hbar \mathcal{L}^{-1}\left\{\frac{1}{s^\alpha}\mathcal{L}\{(f_m)_{\theta\theta\theta\theta} - (f_m^3 - f_m)_{\theta\theta} - \beta(f_m)_\theta\}\right\}. \tag{29}$$

Substituting m = 0 in Eq. (29):

$$f_1(\theta, t, \hbar) = (1-\hbar) f_0(\theta, t) + \hbar f_0(\theta, 0) - \hbar \mathcal{L}^{-1}\left\{\frac{1}{s^\alpha}\mathcal{L}\{(f_0)_{\theta\theta\theta\theta} - (f_0^3 - f_0)_{\theta\theta} - \beta(f_0)_\theta\}\right\}. \tag{30}$$

Mathematica 13.2 can be used to evaluate $f_1(\theta, t, \hbar)$ as follows:

$$f_1(\theta, t, \hbar) = \tanh\left(\frac{\theta}{\sqrt{2}}\right) - \frac{\beta\hbar\left(\sinh\left(\frac{3\theta}{\sqrt{2}}\right) - 11\sinh\left(\frac{\theta}{\sqrt{2}}\right)\right)\operatorname{sech}^5\left(\frac{\theta}{\sqrt{2}}\right)\left(\frac{t^\rho}{\rho}\right)^\alpha}{2\Gamma(\alpha+1)}. \tag{31}$$

Substituting m = 1, the second approximate solution is as follows:

$$f_2(\theta, t, \hbar) = (1-\hbar) f_1(\theta, t) + \hbar f_0(\theta, 0) - \hbar \mathcal{L}^{-1}\left\{\frac{1}{s^\alpha}\mathcal{L}\{(f_1)_{\theta\theta\theta\theta} - (f_1^3 - f_1)_{\theta\theta} - \beta(f_1)_\theta\}\right\}. \tag{32}$$

Accordingly, we derive the following expression for $f_2(\theta, t, \hbar)$:

$$f_2(\theta,t,\hbar) = \tanh\left(\frac{\theta}{\sqrt{2}}\right) + \frac{\beta\hbar t^{\alpha-1}\operatorname{sech}^2\left(\frac{\theta}{\sqrt{2}}\right)}{32\Gamma(\alpha+1)^4}\Big[24\alpha\beta\hbar^2\Gamma(\alpha+1)t^{2\alpha}\Big(-9187\cosh\left(\sqrt{2}\theta\right)+1914\cosh\left(2\sqrt{2}\theta\right)$$
$$-125\cosh\left(3\sqrt{2}\theta\right)+2\cosh\left(4\sqrt{2}\theta\right)+7780\Big)\tanh\left(\frac{\theta}{\sqrt{2}}\right)\operatorname{sech}^{10}\left(\frac{\theta}{\sqrt{2}}\right)-9\alpha\beta^2\hbar^3t^{3\alpha}$$
$$\Big(132934\cosh\left(\sqrt{2}\theta\right)-36952\cosh\left(2\sqrt{2}\theta\right)+4279\cosh\left(3\sqrt{2}\theta\right)-202\cosh\left(4\sqrt{2}\theta\right)+3\cosh\left(5\sqrt{2}\theta\right)$$
$$-102110\Big)\tanh\left(\frac{\theta}{\sqrt{2}}\right)\operatorname{sech}^{14}\left(\frac{\theta}{\sqrt{2}}\right)+16t\Gamma(\alpha+1)^3\Big(\sqrt{2}-4(\hbar-1)\tanh\left(\frac{\theta}{\sqrt{2}}\right)\Big(3\operatorname{sech}^2\left(\frac{\theta}{\sqrt{2}}\right)-1\Big)\Big)$$
$$8\alpha\hbar\Gamma(\alpha+1)^2t^{\alpha}\operatorname{sech}^4\left(\frac{\theta}{\sqrt{2}}\right)\Big(672\sinh\left(\sqrt{2}\theta\right)-\sqrt{2}\beta\left(-26\cosh\left(\sqrt{2}\theta\right)+\cosh\left(2\sqrt{2}\theta\right)+33\right)$$
$$+72\tanh\left(\frac{\theta}{\sqrt{2}}\right)\Big(112\operatorname{sech}^2\left(\frac{\theta}{\sqrt{2}}\right)-107\Big)\Big)\Big]. \tag{33}$$

Extending the process to $m = 2$, 3, and higher yields the approximate solution. However, we restrict our attention to computing $f_2(\theta, t, \hbar)$. The parameter $\hbar$ is essential for ensuring convergence as m grows. To identify the convergence region, we visualize $\hbar$ curves at $\theta = 1.5$ and $t = 0.5$ for different values of α. Table 3 presents a comparison of our approximate solutions, absolute errors for different x values and time steps, and analytical results from [16]. The minimal error confirms the accuracy of the suggested approach.

Table 3: The exact solution in [16] and the numerical approximations of $f(\theta, t)$ presented in Eq. (2) and the error magnitude at $\rho = 1$, $\beta = 0.1$ for $\alpha = 1$ at $\hbar = 0.01$

t	x	Exact	Numerical	$\lvert Error\rvert$
0.1	–10	–0.99999	–0.99999	2.18385×10^{-7}
	–8	–0.99997	–0.99998	3.69473×10^{-6}
	–7	–0.99988	–0.9999	1.51961×10^{-5}
	–5	–0.998045	–0.998302	2.56663×10^{-4}
0.01	–10	–0.99999	–0.99999	2.04703×10^{-8}
	–8	–0.99998	–0.99997	3.46325×10^{-7}
	–7	–0.99989	–0.9999	1.42441×10^{-6}
	–5	–0.99828	–0.99830	2.40611×10^{-5}
0.05	–10	–0.99999	–0.999999	1.0532×10^{-7}
	–8	–0.99997	–0.99997	1.78185×10^{-6}
	–7	–0.99989	–0.9999	7.32862×10^{-6}
	–5	–0.998179	–0.998302	1.23788×10^{-4}

5 Graphical Illustrations

Visual representations play a crucial role in elucidating complex mathematical concepts by offering an intuitive understanding of underlying dynamics. They serve as an effective tool for analyzing the behavior of the studied model, enabling explicit examinations of its properties. Whether in two-dimensional or three-dimensional form, these graphical depictions facilitate direct comparisons between analytical and numerical solutions, while also highlighting the intricate relationships among the governing parameters of the equation. Here, we provide a series of visual representations that confirm the correctness of our obtained solutions.

Fig. 1 presents the results from the FCCMS's approximation (21) for different values of α and t. In Fig. 1a and b, the real parts of $f(\theta, y, \mathrm{t})$ and $g(\theta, y, \mathrm{t})$ are depicted, considering $a = \xi = \eta = 2$, $y = 10$, $\rho = 1$, and $\mathrm{t} = \hbar = 0.5$, with varying α. Figs. 2 and 3 further illustrate the approximate solutions under different parameter values. These graphical illustrations effectively capture the numerical solution's sensitivity to varying parameter values, underscoring the substantial influence of such variations on system behavior. Finally, Fig. 4 provides insight into the $\hbar$ curve for the solution at $\theta = 1$, where $\rho = 0.2$ and $\mathrm{t} = 0.1$. The analysis confirms that the optimal range for $\hbar$ is [–0.2, 1] for f and [–0.6, 0.4] for g, with recommended values of 0.5 and –0.1, respectively. To illustrate the impact of fractional orders on the solutions of Eq. (21), Fig. 5a–d displays the surface structure of imaginary aspects of $f(\theta, y, \mathrm{t})$ for different values of α, specifically 1, 0.9, 0.75, and 0.7, over the interval $-5 \leq \theta \leq 5$ and $0 \leq \mathrm{t} \leq 2$. The obtained solution exhibits periodicity while gradually decaying over time. Notably, the rate of decay increases with rising α. Likewise, Fig. 6a–d illustrates the behavior of $g(\theta, y, \mathrm{t})$ under α =1, 0.9, 0.75, and 0.7 considering $-5 \leq \theta \leq 5$ and $-5 \leq \mathrm{t} \leq 5$. We obtain a bell-shaped soliton solution that aligns well with the analytical solution, confirming how solution dynamics evolve with decreasing α.

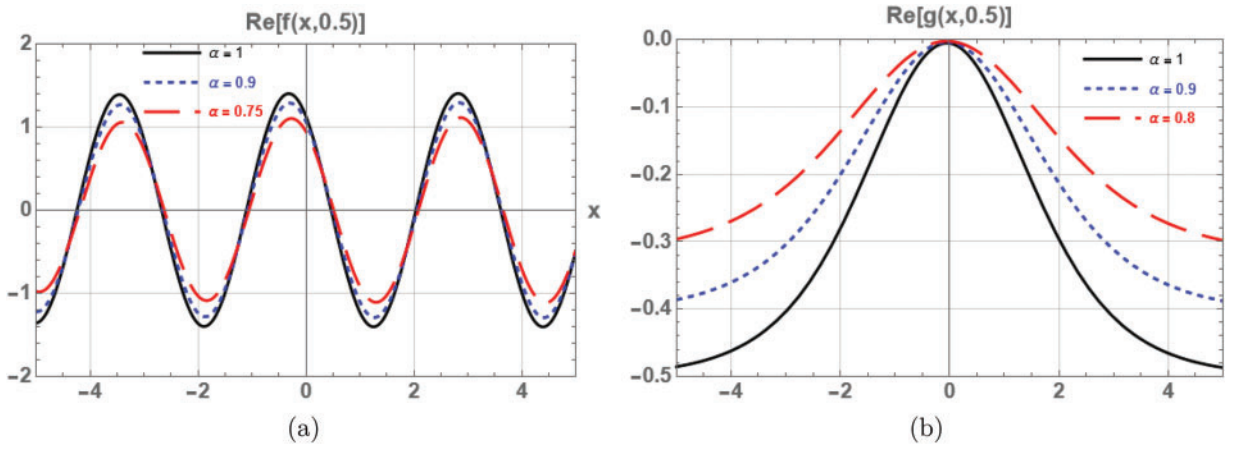

Figure 1: 2D plots of the real parts of $f(\theta, y, \mathrm{t})$ and $g(\theta, y, \mathrm{t})$ for the time-FCCMS (21) at various α values: (a) $Re(f(\theta, y, \mathrm{t}))$ with parameters $a = \xi = \eta = 2$, $y = 10$, $\rho = 1$, and $\mathrm{t} = \hbar = 0.5$. (b) $Re(g(\theta, y, \mathrm{t}))$ with $\mathrm{t} = \xi = \eta = 0.5$, $a = y = 0.05$, $\rho = 0.4$ and $\hbar = -0.1$

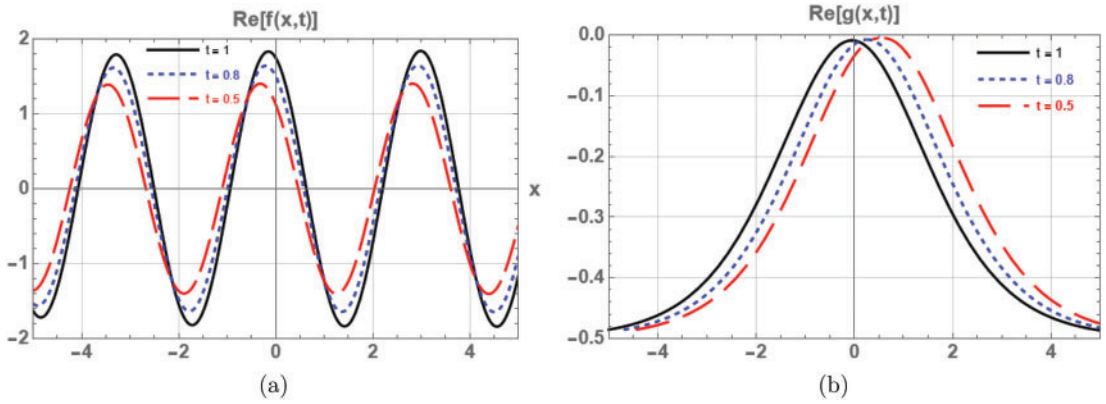

Figure 2: 2D plots of the real parts of $f(\theta, y, \mathrm{t})$ and $g(\theta, y, \mathrm{t})$ for the time-FCCMS (21) at varying values of t: (a) $Re(f(\theta, y, \mathrm{t}))$ for $\alpha = 1$, $a = \xi = \eta = 2$, $y = 10$, $\rho = 1$ and $\hbar = 0.5$. (b) $Re(g(\theta, y, \mathrm{t}))$ for $\alpha = 1$ $\xi = \eta = 0.5$, $a = y = 0.05$, $\rho = 0.4$ and $\hbar = -0.1$

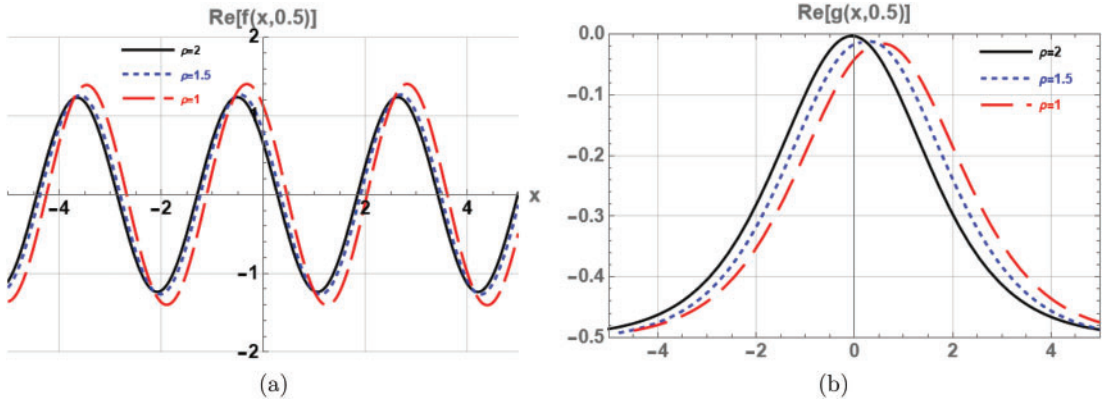

Figure 3: Two-dimensional plots of the real components of $f(\theta, y, \mathrm{t})$ and $g(\theta, y, \mathrm{t})$ for time-FCCMS (21), illustrating the effect of varying ρ: (a) $Re(f(\theta, y, \mathrm{t}))$ for $\alpha = 1$, $a = \xi = \eta = 2$, $y = 10$ and $\mathrm{t} = \hbar = 0.5$. (b) $Re(g(\theta, y, \mathrm{t}))$ for $\alpha = 1\mathrm{t} = \xi = \eta = 0.5$, $a = y = 0.05$ and $\hbar = -0.1$

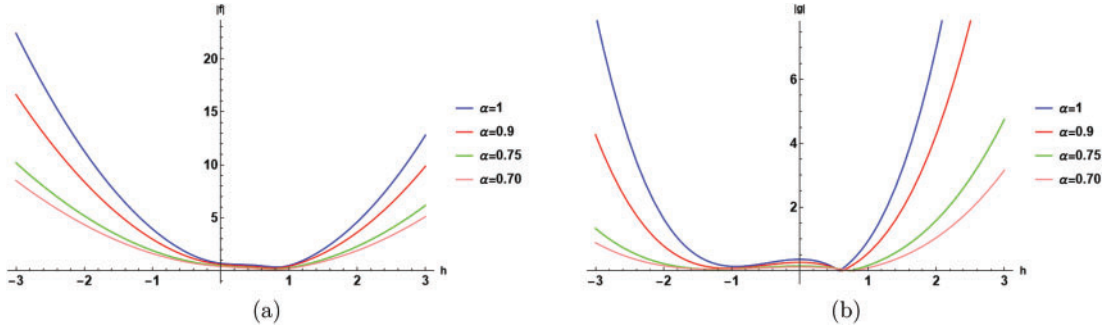

Figure 4: Representation of the $\hbar$ curves corresponding to the solutions, plotted for $\theta = 1$, $y = 1.5$, $\mathrm{t} = 0.1$ with parameters $a = 0.3$, $\xi = 0.5$, $\eta = 0.6$ and $\rho = 0.2$ (a) $\hbar$ curves for $f(\theta, y, t)$ (b) $\hbar$ curves for $g(\theta, y, t)$

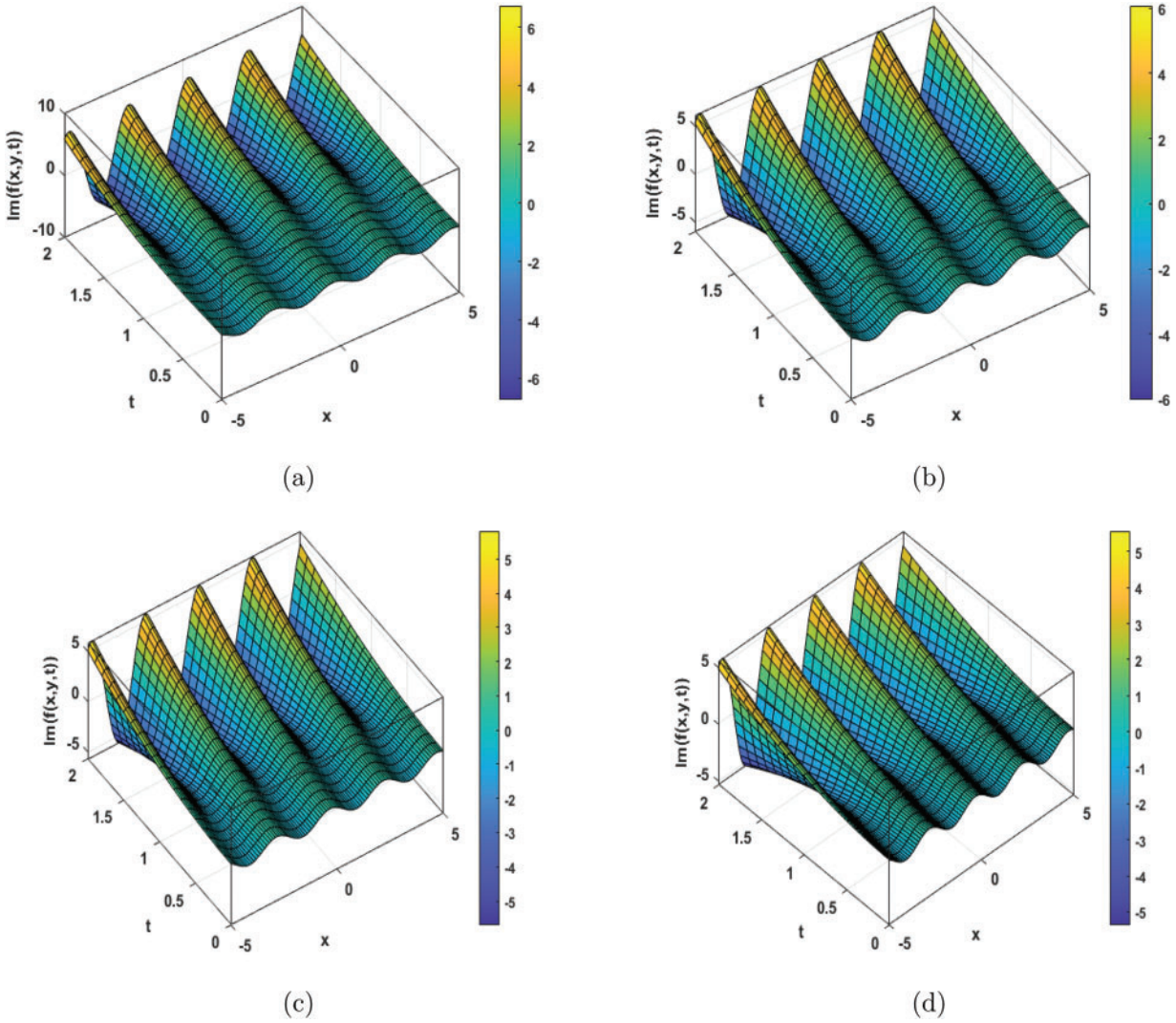

Figure 5: 3D visualizations of $Im(f(\theta, y, \mathrm{t}))$ in the time-FCCMS (21) for $a = 0.05$, $y = 10$, $\xi = 2.5$, $\eta = 1.5$, $\rho = 1$, and $\hbar = 0.3$ at several α values. (a) $\alpha = 1$, (b) $\alpha = 0.9$, (c) $\alpha = 0.75$, (d) $\alpha = 0.7$

Fig. 7 presents the solutions obtained from the approximation of the time-FCHE (2) for a broad range of measurements of α and t. In particular, we look at the cases where $\alpha = 1$, 0.75, and 0.25 with fixed parameters $\rho = 1$ and $\beta = 0.1$. Additionally, Fig. 7b illustrates how the approximate solutions evolve with different values of t, demonstrating a remarkable consistency despite temporal variations. In Fig. 7c, the approximate solutions employing the GCFD in spatiotemporal coordinates for $\alpha = 1$ and $\mathrm{t} = 0.5$ exhibit a strong agreement, regardless of the varying values of ρ. Fig. 7d visualizes the $\hbar$ curves at $\theta = 1.5$, $\rho = 1$ and $\mathrm{t} = 0.5$, for different α, indicating that the suitable extent of $\hbar$ lies in [–0.7, 0.5], with an optimal choice of around 0.01. Also, Fig. 8a–c presents 3D coordinate-space graphs, illustrating kink wave solitons that remain stable under perturbations. These graphs, plotted for varying fractional parameter α, span the domains $-10 \leq \theta \leq 10$ and $0 \leq \mathrm{t} \leq 2$.

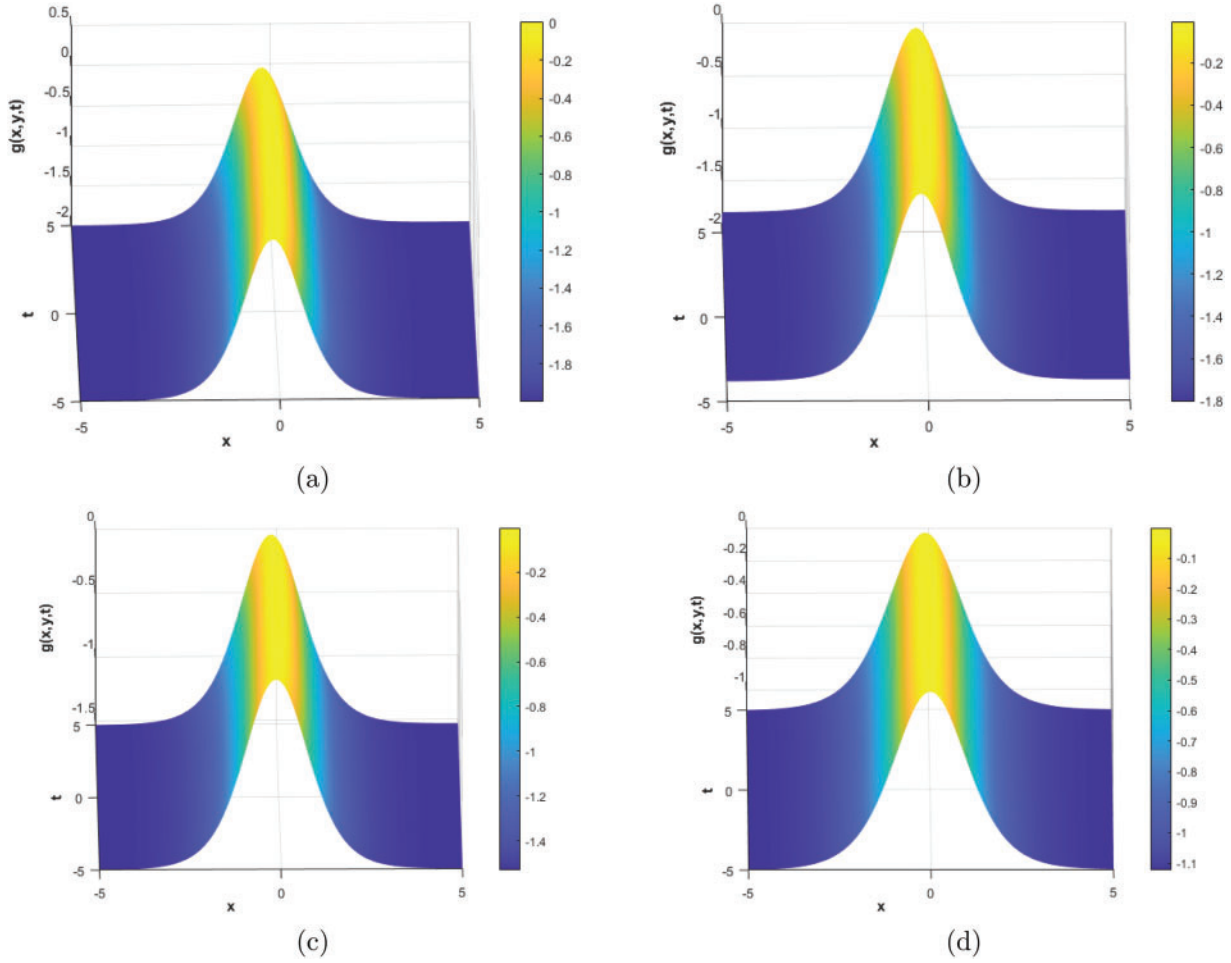

Figure 6: 3D visualizations of $g(\theta, y, \mathrm{t})$ in the time-FCCMS (21) for $a = y = 0.05$, $\xi = 0.01$, $\eta = 0.001$, $\rho = 0.4$, and $\hbar = -0.1$ at various values of α. (a) $\alpha = 1$, (b) $\alpha = 0.9$, (c) $\alpha = 0.75$, (d) $\alpha = 0.7$

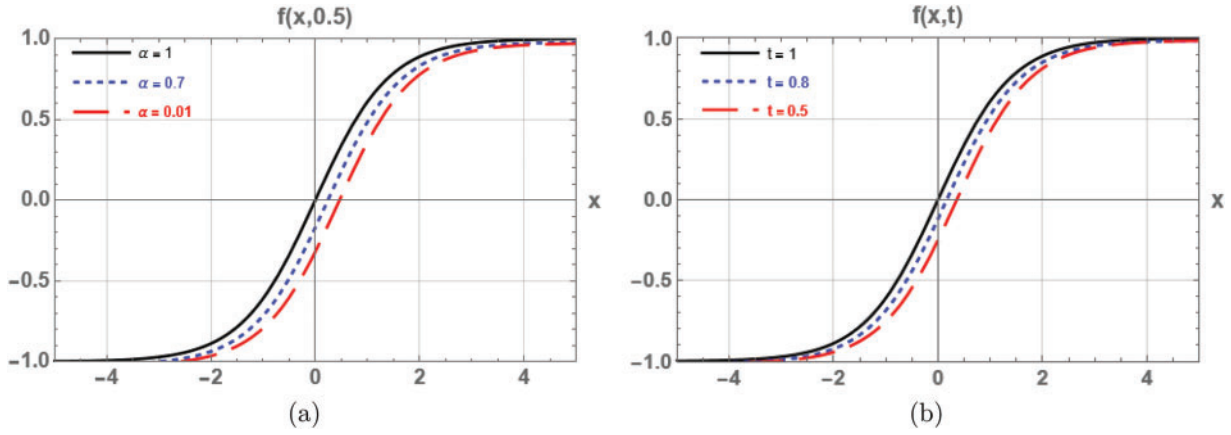

Figure 7: (Continued)

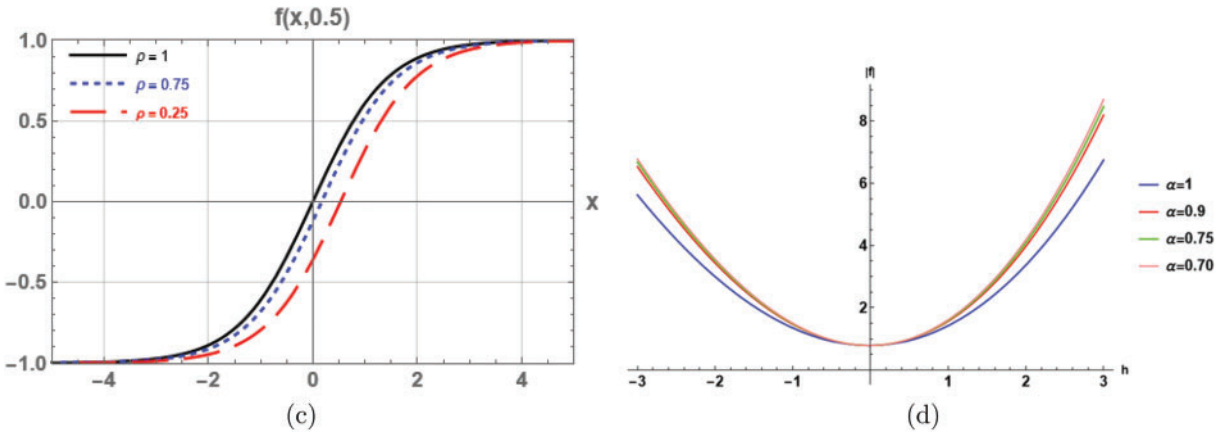

Figure 7: 2D plots of $f(\theta, \mathrm{t})$ for Eq. (2): (a) At $\mathrm{t} = 0.5$, showing variations with α. (b) For different t values. (c) For different ρ values. (d) $\hbar$ curve at $\theta = 1.5, \mathrm{t} = 0.5$, and $\rho = 1$

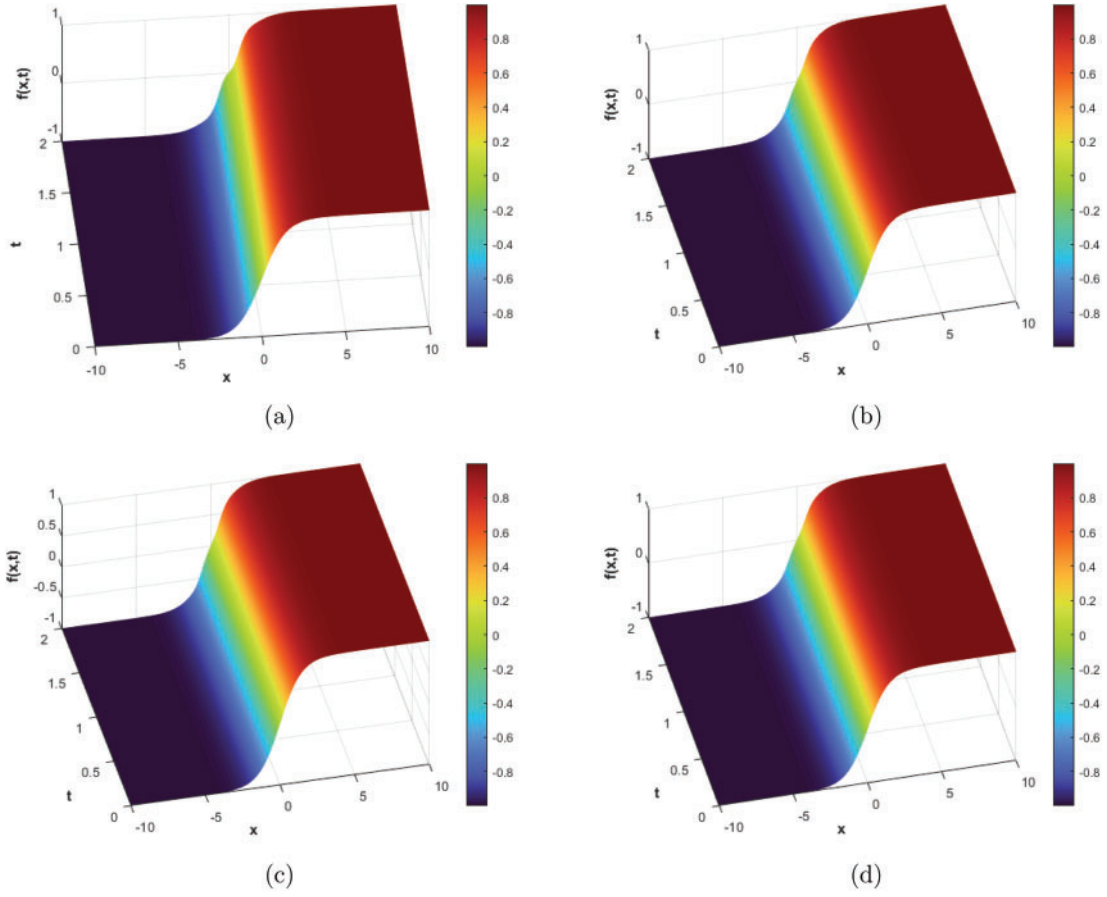

Figure 8: 3D visualizations of $g(\theta, \mathrm{t})$ for the time-FCHE (2) for $\beta = 0.1$, $\rho = 0.2$, and $\hbar = 0.01$ at different values of α. (a) $\alpha = 1$, (b) $\alpha = 0.9$, (c) $\alpha = 0.75$, (d) $\alpha = 0.5$

6 Conclusion

Our investigation involved the use of the CP methodology coupled with the ρ-LT as an innovative solution framework for approximating FCCMS and FCHE. By skillfully integrating the ρ-LT with the CP method, the projected approach efficiently resolved nonlinear fractional problems without relying on Adomian polynomials or Lagrange multipliers. The fractional derivatives were interpreted in the Caputo sense, and convergence was further optimized by incorporating a small parameter, ħ. The method's remarkable accuracy was validated through absolute error tables, with visual demonstrations in the form of graphs reinforcing its effectiveness and reliability. This approach stood out for its precision, efficiency, and simplicity, making it a versatile tool for advancing fractional differential equation studies. While the method proves to be highly effective, it does come with a significant limitation: it converges only under certain initial conditions and tends to work better with initial value problems than with those involving boundary conditions. For future directions, it can be employed to investigate more complex systems that have significant applications in various real-world areas by employing the CP transform method. Through a thorough analysis of these systems, we seek to discover essential properties of the governing equations, which can be used to develop innovative solutions for practical challenges.

Acknowledgement: The authors extend their appreciation to the Deanship of Research and Graduate Studies at King Khalid University, Saudi Arabia for funding this work through the Large Research Project under grant number RGP.2/65/46.

Funding Statement: This research was funded by King Khalid University, Saudi Arabia, Project No. (RGP.2/65/46).

Author Contributions: The authors confirm contribution to the paper as follows: study, conception and design: Nauman Raza; methodology, initial draft: Zuha Khalid and Younes Chahlaoui; analysis and interpretation of results: Zuha Khalid and Muhammad Farman; visualization, edited: Evren Hincal. All authors reviewed the results and approved the final version of the manuscript.

Availability of Data and Materials: All data generated or analyzed in this study are included in this published article.

Ethics Approval: Not applicable.

Conflicts of Interest: The authors declare no conflicts of interest to report regarding the present study.

References

1. Obeidat NA, Bentil DE. New theories and applications of tempered fractional differential equations. Nonlinear Dyn. 2021;105(2):1689–702. doi:10.1007/s11071-021-06628-4.
2. Abd Elbary FE, Ali KK, Semary MS, Abdel-wahed MS, Elsisy MA. A new approach for solving fractional kundu-eckhaus equation and fractional massive thirring model using controlled picard's technique with ρ-laplace transform. Partial Differ Equat Appl Mathem. 2024;10(4):100675. doi:10.1016/j.padiff.2024.100675.
3. Dalir M, Bashour M. Applications of fractional calculus. Appl Math Sci. 2010;4(21):1021–32.
4. Alharbi WG, Ali KK, Mohamed MS, Maneea M. Solving the time fractional q-deformed tanh-gordon equation: a theoretical analysis using controlled picard's transform method. AIMS Math. 2024;9(9):24654–3676. doi:10.3934/math.20241201.

5. Belair J, Engelborghs K, Lemaire V, Roose D. Numerical bifurcation analysis of delay differential equations arising from physiological modeling. J Math Biol. 2001;42(4):361–85. doi:10.1007/s002850000072.
6. Ali KK, Maaty MA, Maneea M. Optimizing option pricing: exact and approximate solutions for the time-fractional ivancevic model. Alex Eng J. 2023;84(2):59–70. doi:10.1016/j.aej.2023.10.066.
7. Cheow YH, Ng KH, Phang C. The application of fractional calculus in economic growth modelling: an approach based on regression analysis. Heliyon. 2024;10(15):e35379. doi:10.1016/j.heliyon.2024.e35379.
8. Debnath L, Basu K. Nonlinear water waves and nonlinear evolution equations with applications. In: Solitons. Cham, Switzerland: Springer; 2022. p. 1–45. doi:10.1007/978-1-0716-2457-9_609.
9. Zhou X, Ilhan OA, Manafian J, Singh G, Tuguz NS. N-lump and interaction solutions of localized waves to the (2+1)-dimensional generalized KDKK equation. J Geom Phys. 2021;168(391):104312. doi:10.1016/j.geomphys.2021.104312.
10. Emmrich E, Feireisl E, Kruse R. Nonlinear stochastic evolution equations: analysis, numerics, and applications; 2018 [cited 2025 Apr 15]. Available from: http://www.math.tu-berlin.de/preprints/files/Preprint-12-2018.pdf. doi:10.14279/depositonce-14672.
11. Maccari A. The kadomtsev-petviashvili equation as a source of integrable model equations. J Mathem Phys. 1996;37(12):6207–12. doi:10.1063/1.531773.
12. Chen Z, Manafian J, Raheel M, Zafar A, Alsaikhan F, Abotaleb M. Extracting the exact solitons of time-fractional three coupled nonlinear maccari's system with complex form via four different methods. Results Phys. 2022;36:105400. doi:10.1016/j.rinp.2022.105400.
13. Ehsan H, Abbas M, Abd El-Rahman M, Ali MR, Hendy AS. The dynamical study of fractional complex coupled maccari system in nonlinear optics via two analytical approaches. Results Phys. 2023;52(1):106775. doi:10.1016/j.rinp.2023.106775.
14. Cahn JW, Hilliard JE. Free energy of a nonuniform system. I. Interfacial free energy. J Chem Phys. 1958;28(2):258–67. doi:10.1063/1.1744102.
15. Kim J. A numerical method for the cahn-hilliard equation with a variable mobility. Commun Nonlinear Sci Numer Simul. 2007;12(8):1560–71. doi:10.1016/j.cnsns.2006.02.010.
16. Ugurlu Y, Kaya D. Solutions of the cahn-hilliard equation. Comput Mathem Applicat. 2008;56(12): 3038–45. doi:10.1016/j.camwa.2008.07.007.
17. Choo SM, Chung SK, Lee YJ. A conservative difference scheme for the viscous cahn-hilliard equation with a nonconstant gradient energy coefficient. Appl Numer Math. 2004;51(2):207–19. doi:10.1016/j.apnum.2004.02.006.
18. Yousaf MZ, Abbas M, Abdullah FA, Nazir T, Alzaidi ASM, Emadifar H. Construction of travelling wave solutions of coupled Higgs equation and the Maccari system via two analytical approaches. Opt Quant Elect. 2024;56(6):967. doi:10.1007/s11082-024-06708-w.
19. Abdelrahman M, Hassan S. New exact solutions for the maccari system. J Phys Math. 2018;9(1):1–7.
20. Hussain S, Shah A, Ullah A, Haq F. The q-homotopy analysis method for a solution of the cahn-hilliard equation in the presence of advection and reaction terms. J Taibah Univ Sci. 2022;16(1):813–9. doi:10.1080/16583655.2022.2119746.
21. Katugampola UN. A new approach to generalized fractional derivatives. arXiv:1106.0965. 2011.
22. Almeida R. A caputo fractional derivative of a function with respect to another function. Commun Nonlinear Sci Numer Simul. 2017;44:460–81. doi:10.1016/j.cnsns.2016.09.006.
23. Jarad F, Abdeljawad T. A modified laplace transform for certain generalized fractional operators. Res Nonlinear Analy. 2018;1(2):88–98.

24. Abdeljawad T. On conformable fractional calculus. J Comput Appl Math. 2015;279(182):57–66. doi:10.1016/j.cam.2014.10.016.
25. Semary MS, Hassan HN, Radwan AG. Single and dual solutions of fractional order differential equations based on controlled picard's method with simpson rule. J Assoc Arab Univ Basic Appl Sci. 2017;24(1): 247–53. doi:10.1016/j.jaubas.2017.06.001.